Uncertainty Quantification for Computational Modelling of Laser Powder Bed Fusion

S Wells[1,4], A Plotkowski[2], J Coleman[2], M Rolchigo[2], R Carson[3], and M J M Krane[1]

[1]Purdue Center of Metal Casting Research; School of Materials Engineering, Purdue University, West Lafayette, IN 47907, USA
[2]Oak Ridge National Laboratory, Oak Ridge, TN 37830, USA
[3]Lawrence Livermore National Laboratory, Livermore, CA 94550, USA
[4]currently Continuous Casting Consortium; Department of Mechanical Engineering, Colorado School of Mines, Golden, CO 80401, USA

Wells130@purdue.edu

Abstract. Additive manufacturing (AM) may have many advantages over traditional casting and wrought methods, but our understanding of the various processes is still limited. Computational models are useful to study and isolate underlying physics and improve our understanding of the AM process-microstructure-property relations. However, these models necessarily rely on simplifications and parameters of uncertain value. These assumptions reduce the overall reliability of the predictive capabilities of these models, so it is important to estimate the uncertainty in model output. In doing so, we quantify the effect of model limitations and identify potential areas of improvement, a procedure made possible by uncertainty quantification (UQ). Here we highlight recent work which coupled and propagated statistical and systematic uncertainties from a melt pool transport model based in OpenFOAM, through a grain scale cellular automaton code. We demonstrate how a UQ framework can identify model parameters which most significantly impact the reliability of model predictions through both models and thus provide insight for future improvements in the models and suggest measurements to reduce output uncertainty.

1. Introduction

Additive manufacturing of metal alloys such as Ti-6Al-4V, 316 SS, IN625, and IN718 [1] is a class of metallurgical processes whereby components are printed in a layer-by-layer manner directed by a digital model of the part. Laser powder bed fusion (L-PBF) involves laser melting and localized consolidation of metal powders at sub-millimeter length scales, allowing for the production of complex components difficult to produce via more traditional casting or deformation processing. As such, metal additive manufacturing has found applications in aerospace, automotive, and biomedical fields [2]; yet detrimental defects and inconsistent build quality and performance [3-7] make certification of critical components difficult and limit industrial adaptation. Given the potential upsides of AM, reducing these defects and thus broadening the applicability of the process is at the forefront of ongoing research efforts. However, process complexity, laser system costs, and material costs mean experimental studies are difficult. Computational models offer a supplementary means of investigating the process while allowing for reproducibility and isolation of underlying physics.

Unfortunately, the complexity and scale of influential physics involved in metal additive manufacturing is too great to be captured by a single computational model. Instead, multiple models

which specialize in a particular physical phenomenon must be developed and coupled to fully capture the process. Examples of computational models for AM research include melt pool transport models such as those used in [8-12], which provide temperature history data and melt pool geometries to aid in the development of scan strategies [13]. Also, microstructure evolution models [14-17] are vital for understanding as-built microstructures and crystal plasticity codes [18-21] predict the constitutive mechanical behavior. While computational models such as these are powerful tools to investigate and provide insight into metal additive manufacturing, their practical use relies on trade-offs between computational efficiency and model fidelity which reduce overall reliability of their predictions. Additionally, the data used to drive simulations (e.g., thermophysical properties) have inherent uncertainty that propagate to simulation results. It is therefore important to quantify the reliability of model predictions and the uncertainty therein, a process made possible via uncertainty quantification (UQ).

Two types of uncertainty are present in computational models such as those used for AM research, both of which must be considered. The first is statistical uncertainty, referred to as *aleatoric uncertainty*, resulting from natural variations in observations or measurements, oftentimes resulting from the equipment making the measurements. Aleatoric uncertainty is typically easy to quantify and therefore the propagation to model predictions can be readily determined. The second type of uncertainty is systematic uncertainty, referred to as *epistemic uncertainty*, resulting from a lack of knowledge due to data scarcity or model form error due to simplifications or non-physical parameters. Epistemic uncertainty can only be inferred, and correlations must be drawn. Given the role of simulation in AM research, it is vital that both forms of uncertainty and their propagation be accounted for, and their influences understood to quantify model limitations as well as identify potential areas of improvement.

The present work highlights a few key results from recent studies where an uncertainty quantification framework developed using TASMANIAN [22-26] was applied to two coupled models, a finite volume transport model based in OpenFOAM [9] and ExaCA [27], a cellular automata model for grain scale solidification, to demonstrate how both aleatoric and epistemic uncertainties can be studied and their influence quantified.

2. Methodology

The present work focuses on key findings from two separate studies. The first looks at uncertainty in solidification dynamics resulting from the role of solidification pathway selection. Second, the uncertainty in solidification dynamics is propagated to the as-built microstructure, specifically the grain morphology. The results presented here summarize a few key observations which are more thoroughly detailed in [29].

2.1. Melt Pool Transport Model

The melt pool transport model detailed in this work is based in OpenFOAM for simulations of laser powder bed fusion of Inconel 625 [9]. This model treats the domain as a continuum with volume-weighted thermophysical properties for all phases present in a computational cell.

2.1.1. Conservation Equations. The transport model solves the conservation of mass, momentum, and energy equations. In the present studies, fluid flow driven by Marangoni effects are disregarded and therefore the conservation of mass and momentum can be disregarded leaving only the conservation of energy given by Eqn. (1),

$$\rho C_p \frac{\partial T}{\partial t} = \nabla \cdot (k \nabla T) + S_T + \dot{Q} \tag{1}$$

where ρ is density, t is time, C_P is the specific heat capacity, T is temperature in Kelvin, and k is the thermal conductivity of IN625. S_T is an energy source term given by Eqn. (2) which accounts for the evolution of latent heat release due to phase change.

$$S_T = -\rho L_f \frac{\partial f_l}{\partial t} \quad (2)$$

$\dot{Q}$ is a volumetric laser heat source given by Eqn. (3) where η is the laser absorption efficiency, P is laser power, r is the laser radius and d is the penetration depth over which the laser energy is integrated. x, y, and z are the laser center location and x_b is the laser center starting point.

$$\dot{Q}(x,y,z) = \frac{2\eta P}{r^2 d(\pi/3)^{3/2}} \exp\left(\frac{-3((x - x_b) + y)^2}{r^2} + \frac{-3z^2}{d^2}\right) \quad (3)$$

2.1.2. Boundary Conditions. For the present model, radiative heat transfer along the top boundary is governed by a heat transfer coefficient h given by Eqn. (4), and vaporization by heat flux (q''_v) given

$$h = \varepsilon\sigma(T^4 - T_\infty^4) \quad (4)$$

$$q''_v = A \cdot \frac{\exp\left(B - \frac{C}{T}\right)}{\sqrt{T}} \quad (5)$$

by Eqn. (5). Here ε is emissivity, σ is the Stefan-Boltzmann coefficient, T_∞ is the far field temperature taken to be 300K, and A, B, and C are algebraic coefficients. Input parameter values are provided in Table 1.

2.1.3. Simulation Domain, Time Step, and Grid Spacing. In the presented results two different simulation domains were used. A single line scan was used in Section 3.1 with a domain size of 5.0 x 0.8 x 0.4 mm to ensure a steady state melt pool was established at the probe locations while still approximating a semi-infinite domain surrounding the melt pool. In Section 3.2 and 3.3 a multi-pass, multi-layer simulation based on the AMB2018-01 test bed series [30] was used to create a build volume over which the microstructure was analyzed. This consists of alternating even/odd scan pattern totalling 65 layers. For both simulation domains a uniform grid spacing of 5 μm was used to ensure sufficient spatial resolution needed to capture the melt pool curvature. A 0.1 μs timestep was used for the single line scan, while an adaptive timestep was used for the multi-pass multi-layer simulation to reduce simulation time when the laser is off during dwell periods.

2.1.4. Outputs of Interest. For the single line scan study, the output of interest is the cooling rate through the tail of the melt pool along the top surface defined by a relative position through the mushy zone (x_{rel}) where $x_{rel} = 0$ at the liquidus isotherm and $x_{rel} = 1$ at the solidus isotherm. For the coupled models study, the outputs of interest were selected based on the inputs required by the weakly coupled CA grain scale solidification model. Here, the time at which each computational cell drops below the liquidus temperature and the instantaneous cooling rate at the liquidus isotherm are recorded and passed to ExaCA.

2.2. CA Grain Growth Model

2.2.1. Initialization. The grid spacing used by the transport model is too coarse to adequately resolve grain competition and nucleation, therefore the OpenFOAM temperature data was interpolated down to the CA grid spacing (2.5 μm here). Additionally, a substrate was simulated using a substrate grain size S_0 which was then used to calculate the number of grains (and thus grain seeds) in the substrate. Each grain seed was assigned to a random cell in the substrate with 1 of 10,000 possible cubic grain

orientations. Cells not assigned a seed were grouped to the nearest seed to develop the final substrate grain structure..

2.2.2. Grain Growth. The decentered octahedron method is leveraged by ExaCA [27] which tracks the solidification front as it grows. An octahedral grain envelope half-diagonal direction, each half-diagonal aligned with one of the <001> crystallographic directions) is assigned to each active cell. During each time step where an active cell has a temperature below the liquidus, the half-diagonal length L of each octahedron is updated using Eqns. (6) and (7).

$$\Delta L = \frac{\Delta t}{\Delta x}(V(\Delta T)) \tag{6}$$

$$V(\Delta T) = \mathbf{A}(\Delta T)^3 + \mathbf{B}(\Delta T)^2 + \mathbf{C}(\Delta T) \tag{7}$$

Here, ΔL is the increment in octahedron half-diagonal length, Δt is the CA timestep, Δx is the grid spacing, and ΔT is the cell undercooling relative to the liquidus temperature. **A**, **B**, and **C** are fitting constants for a polynomial fit to experimental dendrite growth velocities $V(\Delta T)$ based on work by [30]. The octahedron half-diagonal length governed by Eqn. (6) was limited to 0.05 to prevent an order of iteration dependence growth. A timestep of 0.1μs was used to ensure the growth limit is not reached by the advancing melt pool periphery during steady state.

2.2.3. Heterogeneous Nucleation. In addition to grain growth, heterogeneous nucleation ahead of the front is modelled by ExaCA. All cells that will undergo solidification were assigned a random number $R_{nucleation}$ between 0 and 1. In Eqn. (8) N_0 is a heterogeneous nucleation site density. If Eqn. (8) is true, then the cell is a potential nucleation site.

$$R_{nucleation} < N_0(\Delta x)^3 \tag{8}$$

Each cell is then assigned a nucleation undercooling value sampled from a Gaussian distribution centered around ΔT_N with a standard deviation of ΔT_σ. If the nucleation undercooling value of a cell is reached prior to the cell becoming active via a cell capture event associated with grain growth, the nucleation event is successful, a new grain envelope with a random orientation is assigned to the cell, and the cell becomes active. All input parameter values used by the CA model are provided in Table 2.

2.2.4. Outputs of Interest. The grain growth model was used to produce as-built microstructures resulting from temperature data produced by the transport model. The presented work was focused on grain size and shape and thus the outputs of interest were 1) grain misorientation relative to the +Z axis, 2) average grain count, 3) volume weighted aspect ratio, and 4) average grain diameter of a sphere with the same volume. All these values were calculated in a representative value element (RVE) taken out of the middle of the as-built microstructure as depicted in Figure 1.

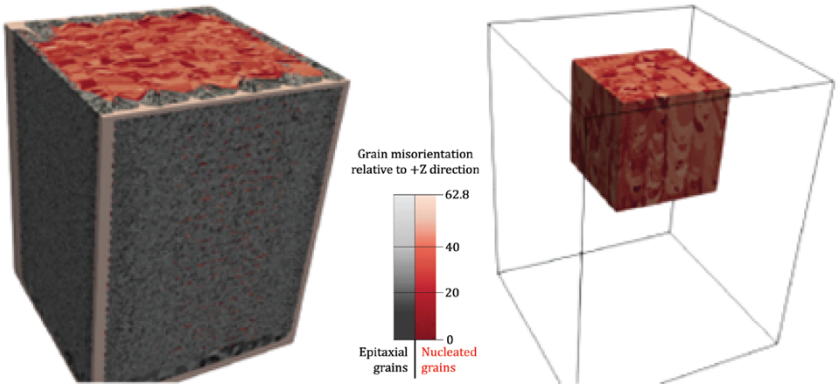

Figure 1. Representative volume element out of which the grain morphology data is drawn. The RVE avoids simulation boundaries and is taken near the top of the build when the microstructure is assumed to fully evolved. Gray indicates epitaxial grains and red grains are nucleated.

2.3. Uncertainty Quantification

To determine the influences of aleatoric and epistemic uncertainties on model reliability, the uncertainty quantification framework detailed in [11] was leveraged here for the analysis of solidification pathway selection using TASMANIAN[21-25].. This framework involves first establishing uncertainty bounds for each input parameters from the literature where possible, or by inference when not. A sensitivity analysis then revealed how the uncertainty in each parameter propagates and manifests as uncertainty in the outputs of interest. In doing so, not only can the most significant contributing uncertainties be determined, but so too can those which are negligible and can be disregarded to simplify the uncertainty space. Next, a sparse grid, which only features the parameters with the highest sensitivity, was constructed where grid points correspond to sets of simulation input parameters. Simulation results corresponding to these points are then used to construct a polynomial response surface. This response surface acts as a surrogate model which approximates the behavior of the computational model/models but can be interrogated rapidly. By sampling the surrogate 10 million times via a Monte Carlo based method, probability density functions (PDFs) are formed. These PDFs represent the uncertainty distribution for each output of interest due to the uncertainty in the considered input parameters.

Table 1. Transport model input parameters and associated uncertainties.

Parameter	Most likely value	Uncertainty	Units
$\rho_{s,l}$	7670.0	1.0%	kg/m^3
$C_{p,s}$	579.28	4.0%	J/(kg K)
$C_{p,l}$	750.65	4.0%	J/(kg K)
k_s	8.275 + 0.01472T	5.0%	J/(m s K)
k_l	4.889 + 0.01474T	5.0%	J/(m s K)
P	195.0	4.5 W	W
η	0.30	15.0%	---
d	20	25.0%	μm
r	85.7	---	μm
L_f	2.18×10^5	4.0%	J/kg
L_v	6.10×10^6	4.0%	J/kg
ε	0.40	---	---
A	2.121×10^{10}	---	$W\ K^{1/2}/m^2$
B	14.29	---	---
C	44,756	---	K

Table 2. Input parameter values and associated uncertainties for the CA grain growth model.

Parameter	Most likely value	Uncertainty	Units
S_0	25.0	10.0μm	μm
ΔT_N	20.0	75%	K
ΔT_σ	2	2K	K
A	-1.0302×10^{-7}	50%	$m/(s\ K^3)$
B	1.0533×10^{-4}	50%	$m/(s\ K^2)$
C	2.2196×10^{-3}	50%	m/(s K)
N_0	10^{15}	---	m^{-3}

3. Results and Discussion

3.1. Influence of Solidification Pathway Selection on Solidification Dynamics

One common assumption made in additive manufacturing modelling is that, due to the cooling rates and melt pool size, transport models lack the necessary resolution to resolve the release of the latent heat profile in the mushy zone and therefore any $f_s(T)$ function used in Eqn. (2) can be used if the entirety of the latent heat is accounted for. For this reason, in addition to thermodynamic models such as equilibrium or Scheil, non-physical but numerically convenient linear or sigmoidal functions (shown for IN625 in Figure 2) are oftentimes used. If the 'lack of resolution' assumption does not hold, then selection of the solidification pathway and latent heat release profile will impact model prediction reliability by increasing the uncertainty therein.

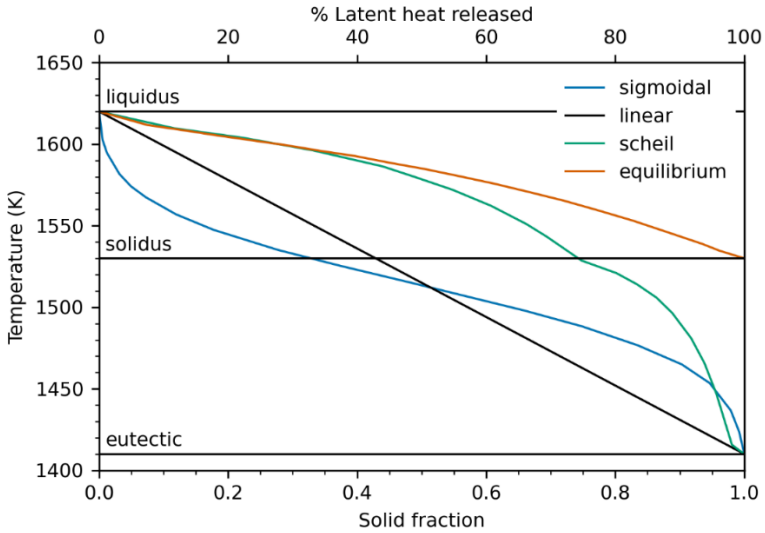

Figure 2. Common solidification pathways which dictate the release of latent heat during solidification.

Using the UQ framework and sensitivity analysis detailed [11], a 3-dimensional sparse grid was constructed for each of the solidification pathways which accounts for the uncertainty in laser absorption efficiency, and solid and liquid specific heat capacities of IN625 (the three parameters model predictions had the highest sensitivity to). 19 simulations were run using each of the pathways and used to construct polynomial response surfaces which act as surrogate models. All four surrogate models were sampled 10-million times to generate the statistics presented in Table 3. These statistics represent the uncertainty in model predictions due to the uncertainty in input parameters. Comparing results for each model illustrates the epistemic uncertainty associated with the solidification pathway selection. Differences

between the pathways indicates that the lack of resolution assumption does not hold for the melt pool length or cooling rate at the liquidus isotherm.

Table 3. Probability density function statistics generated by sampling polynomial surrogate models 10 million times. Differences between the model indicates the lack of resolution assumption does not hold for melt pool length and cooling rate.

Output	Solidification pathway	Mean	2σ
Width [µm]	Scheil	140.91	2.10
	Equilibrium	134.01	2.15
	Linear	140.35	2.10
	Sigmoidal	140.42	2.08
Depth [µm]	Scheil	46.21	1.28
	Equilibrium	42.48	1.28
	Linear	45.84	1.26
	Sigmoidal	45.93	1.26
Length [µm]	Scheil	404.91	14.72
	Equilibrium	370.85	13.86
	Linear	418.22	15.38
	Sigmoidal	417.91	15.34
Cooling rate [K/s]	Scheil	418,751	27,015
	Equilibrium	360,329	19,112
	Linear	923,000	56,035
	Sigmoidal	1,632,218	76,071

In addition to the statistic provided above, Figure 3 depicts the cooling rate through the mushy zone at the tail of the melt pool. If the latent heat release profile were not adequate resolved, these curves would overlap significantly. However, this figure shows how the linear (black) and sigmoidal (blue) predict larger cooling rates near the liquidus isotherm ($x_{rel} = 1$) relative to the equilibrium and Scheil thermodynamic relations, but lower cooling rates near the end of solidification. Figure 2 shows how sigmoidal and linear release a significant amount of latent heat near the onset of solidification, but much less later, whereas sigmoidal and linear are more gradual in their latent heat release throughout the freezing range. These observations agree with those drawn from the surrogate model sampling as the latent heat release profile influences the solidification dynamics.

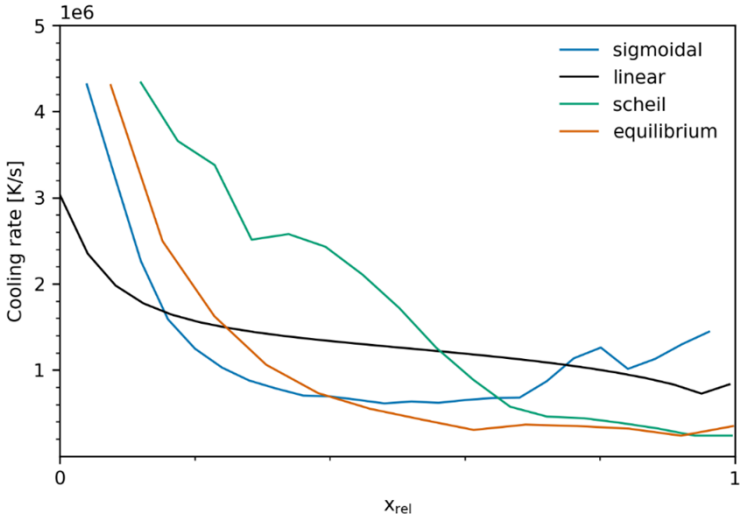

Figure 3. Cooling rate throughout the mushy zone for each of the solidification pathways. Sigmoidal and linear predict higher cooling rates early on, but lower near the end of solidification.

3.2. Grain Morphology Sensitivity Analysis

To begin the uncertainty propagation, a sensitivity analysis was conducted where input parameters for each model were individually adjusted by the uncertainties reported in Tables 1 and 2. These sensitivities are depicted in Figure 4 for each of the outputs of interest. Uncertainty in the interfacial response function coefficients (V(T)), the mean nucleation undercooling temperature, and the laser absorption efficiency showed the highest sensitivities and therefore were included in the surrogate model construction. All other input parameter uncertainties were neglected.

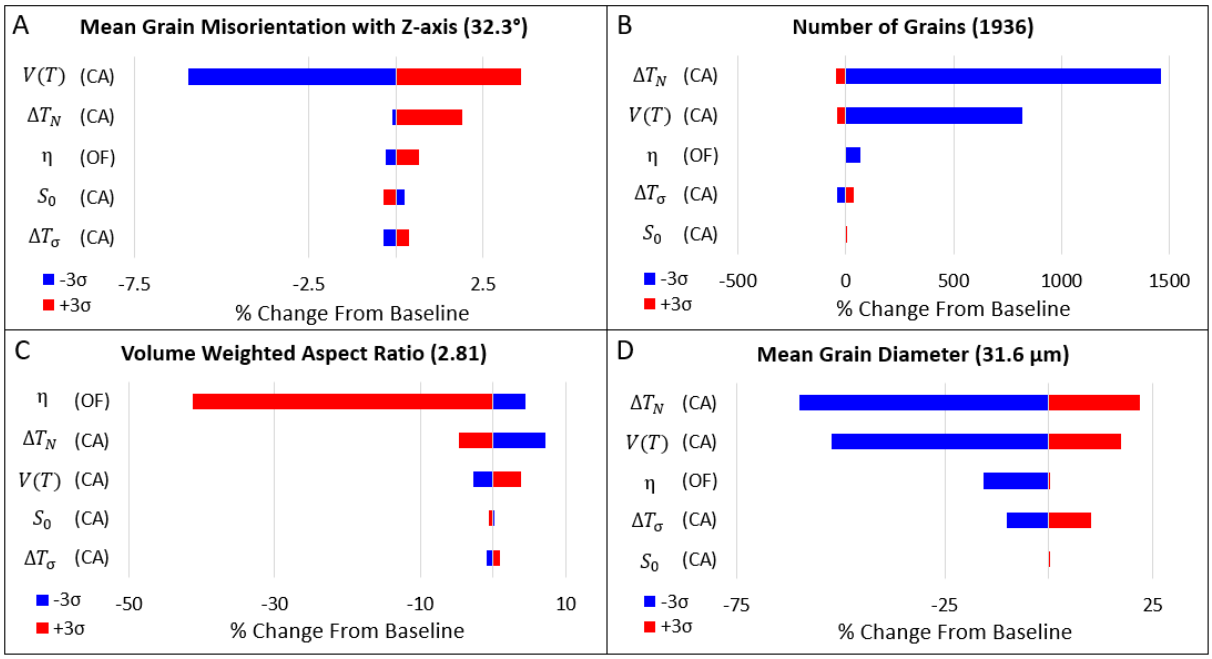

Figure 4. Sensitivity analysis for grain morphology showing uncertainty in laser absorption efficiency, IRF, and the mean nucleation undercooling temperature propagate significantly through the models.

3.3. Influence of Solidification Pathway on Grain Morphology

To determine the extent of uncertainty in grain morphology resulting from the solidification pathway assumption, temperature data from the OpenFOAM transport model for the linear and Scheil solidification pathways was propagated to ExaCA to generate an explicit microstructure. The equilibrium and sigmoidal relations were not carried forward to reduce the total number of simulations. A new 3D sparse grid was generated which included the uncertainty in laser absorption efficiency, mean undercooling for heterogeneous nucleation, and the coefficients dictating the interfacial response function. Surrogate models were generated for the linear and Scheil relations for each of the grain morphology outputs of interest discussed above. Sampling these surrogate models 10-million times produced the statistics presented in Table 4 and show a dependence of the microstructure on the solidification pathway.

Additionally, the probability density functions for the two latent heat release profiles are given in Figure 5**.** Differences between the curves can be attributed to the latent heat release profile through the mushy zone. These results indicate that the solidification pathway selection does impact the predicted as-built grain morphology, yet the significant overlap indicates that the influence is fairly small.

Table 4. Statistical generated by sampling the polynomial surrogate models 10-million times.

	Mean misorientation with Z-Axis [°]	2σ	Number of grains	2σ	Volume weighted aspect ratio	2σ	Mean grain diameter [µm]	2σ
Scheil	33.2	1.69	3,910	12,100	2.75	0.124	31.4	11.1
Linear	32.3	1.10	4,290	12,700	2.76	0.343	30.2	11.4

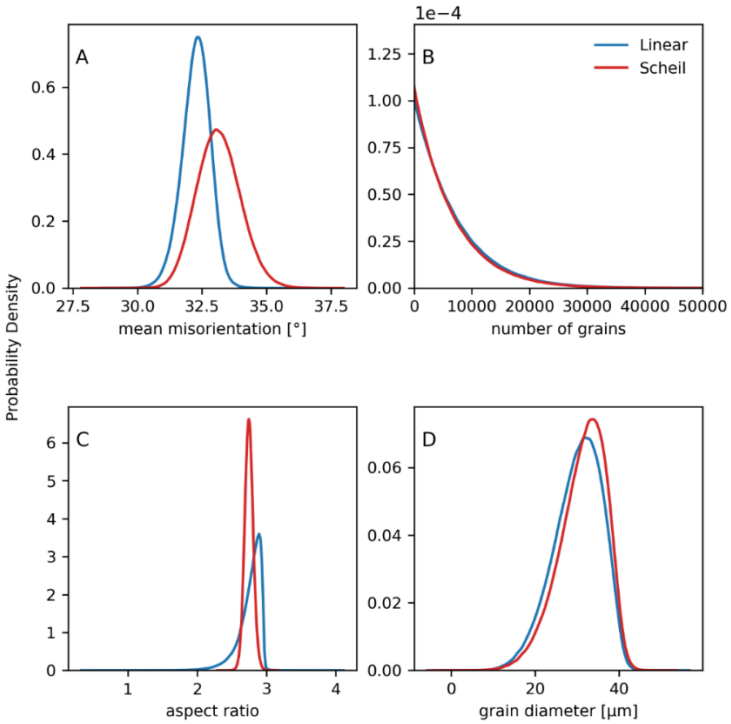

Figure 5. Probability density functions for grain morphology data showing a dependence on the solidification pathway selected.

4. Concluding Remarks

The results presented here are from a series of studies which investigated how statistical and systemic uncertainties impact the reliability of computational model predictions. Key observations from this work include:

- Uncertainty quantification frameworks such as that discussed in [11] allow for critical examination of modelling assumptions and their impact on model performance.
- The lack of resolution assumption often made in additive manufacturing modelling may not hold in the tail of the melt pool where mushy zone thickness is the greatest. When the assumption does not hold, selection of the solidification pathway may impact solidification dynamics and therefore the reliability of model predictions.
- Uncertainty in solidification dynamic predictions arising from the solidification pathway selection were shown to propagate to the predictions of as-built microstructure thus further reducing the reliability of model predictions.
- Lastly, while the results here only include a melt pool transport and cellular automaton grain growth model, it will be important to include a crystal plasticity code such as ExaConstit [27] to fully encompass the process-microstructure-property relations in future propagation studies.

This work was supported by the Exascale Computing Project (17-SC-20-SC), a collaborative effort of the U.S. DOE Office of Science and the NNSA. This manuscript has been authored by UT-Battelle, LLC under Contract No. DE-AC05-00OR22725 with the U.S. Department of Energy. The United States Government retains and the publisher, by accepting the article for publication, acknowledges that the United States Government retains a non-exclusive, paid-up, irrevocable, world-wide license to publish or reproduce the published form of this manuscript, or allow others to do so, for United States Government purposes. The Department of Energy will provide public access to these results of federally sponsored research in accordance with the DOE Public Access Plan (http://energy.gov/downloads/doe-public-access-plan).

References

[1] T DebRoy, H Wei, J Zuback, T Mukherjee, J Elmer, J Milewski, A Beese, A Wilson-Heid, A De, W Zhang 2018 *Prog. Mater. Sci.* **92** 112-224
[2] T Horn, O Harrysson 2012 *Sci. Prog*. **95** 255-282
[3] I Yadroitsev, I Smurov 2011 *Phys. Proc.* **12** 264-270
[4] W King, H King, V Castillo, G Gallegos, J Gibbs, D Hahn, C Kamath, A Rubenchik 2014 *J. Mater. Proc. Tech.* **214** 2915-2925
[5] A Martin, N Calta, S Khairallah, J Wang, P Depond, A Fong, V Thampy, G Guss, A Kiss, K Stone, C Tassone, J Nelson Weker, M Toney, T van Buuren, M Matthews 2019 *Nat. Comm.* **10** 1-10
[6] S Coeck, M Bisht, J Plas, F Verbist 2019 *Add. Manuf.* **25** 347-356
[7] T Mukherjee, W Zhang, T DebRoy 2017 *Comput. Mater. Sci.* **126** 360-372
[8] N Contuzzi, S Campanelli, A Ludovico 2011 *Intern. J. Simul. Mod.* **10** 113-121
[9] J Coleman, A Plotkowski, B Stump, N Raghavan, A Sabau, M Krane, J Heigel, R Ricker, L Levine, S Babu 2020 *J. Heat Transf.* **142** 122201
[10] N Hodge, R Ferencz, J Solberg 2014 *Comput. Mech.* **54** 33-51
[11] S Wells, A Plotkowski, M Krane 2021 *Metall. Mater. Trans. B* **52** 3016-3031
[12] S Khairallah, A Anderson 2014 *J. Mater. Proc. Tech.* **214** 2627-2636
[13] W Yan, W Ge, Y Qian, S Lin, B Zhao, W Liu, F Lin, G Wagner 2017 *Acta Mater* **134**
[14] O Zinovieva, A Zinoviev, V Ploshikhin 2018 *Comput. Mater. Sci.* **141** 207-220
[15] Y Zhang, J Zhang 2019 *Add. Manuf.* **28** 750-765
[16] M Rolchigo, R Carson, J Belak 2022 *Metals* **12** 1-26
[17] X Gong, K Chou 2015 *JOM* **67** 1176-1182
[18] Y Aoyagi, K Shizawa 2007 *Intern. J. Plast.* **23** 1022-1040
[19] M Zhang, J Zhang, DL McDowell, R Neu 2006 *Ninth Intern. Fatigue Congress.*
[20] H Lim, F Abdeljawad, S Owen, B Hanks, J Foulk, C Battaile: (2016), *Modell and Simul in Mater Sci and Engin* **24**
[21] T W Heo, S Khairallah, R Shi, J Berry, A Perron, N Calta, A Martin, N Barton, J Roehling, T Roehling, J Fattebert, A Anderson, A Nichols, S Wopschall, W King, J McKeown, M Matthews 2021 *J. Phys.: Mater.* **4**
[22] M Stoyanov, C. Webster 2016 *Comput. Math. Appl.* **71**
[23] M. Stoyanov 2018 *Lect. Note. Comput. Mater. Sci. Eng.* **123**
[24] M. Stoyanov 2015 *User Manual: TASMANIN Sparse Grids*
[25] Z Morrow M Stoyanov 2020 *SIAM J. Sci. Comput.* **42**
[26] M Stoyanov, D Munster, D Lebrun-Grandie, J Burkardt 2013 https://github.com/ORNL/Tasmanian
[27] M Rolchigo, S Reeve, B Stump, G Knapp, J Coleman, A Plotkowski, J Belak 2022 *Comput. Mater. Sci.* **214** 111692
[28] R Carson, S Wopschall, J Bramwell 2019 https://github.com/LLNL/ExaConstit
[29] S Wells 2022 Uncertainty Quantification of Laser Powder Bed Fusion Computational Models Ph.D. Purdue University Graduate School
[30] J Heigel, B Lane, L Levine, T Phan, J Whiting 2020 *J. Res. Nation. Instit. Stand. Tech.* **125** 1-17
[31] A Rai, M Markl, C Körner 2016 *Comput. Mater. Sci.* **124** 37-48